THERMOCHRONOLOGY OF THE DEEP CRUST IN THE NORTHERN RUBY MOUNTAINS, NV

By
Carlton Mueller
Department of Geological Sciences
University of Colorado at Boulder

April 8, 2019

Thesis Advisor:
Research Associate James Metcalf, Department of Geological Sciences

Defense Committee
Professor Rebecca Flowers, Department of Geological Sciences
Assistant Professor Brian Hynek, Department of Geological Sciences
Senior Instructor Douglas Duncan, Department of Astrophysical & Planetary Sciences

Abstract:

The Mesozoic to Cenozoic transition from contraction to extension of the lithosphere in the western U.S. Cordillera is incompletely constrained due to competing interpretations based on low or high temperature thermochronometers. High temperature thermochronometers, petrological relationships, structural field relations, and P-T-t paths signal a long-lived and older period of extension and exhumation starting in the late-Cretaceous to Oligocene; whereas, competing theories from the analysis of low temperature thermochronometers, and analysis of extensional basins, suggest the onset of extension began mid-Miocene. In the following study, we use low temperature thermochronometers consisting of the apatite and zircon (U-Th)/He systems to analyze an extensional, mylonitic shear zone and exhumed metamorphic core complex within the Ruby Mountains, Nevada. Analysis of 28 zircons from the northern Ruby Mountains, NV depict time of rapid exhumation may have occurred ~17 Ma. Apatites and zircons derived over a 6 km east-west transect, from late-Cretaceous to mid-Cenozoic in age leucogranites, provide an age elevation transect that records exhumation and extension. Our data show a late-Oligocene to early Miocene exhumational history with zircon age dates ranging from 23.5 ± 0.7 to 12.1 ± 0.8 Ma while apatite ages span 18.5 ± 1.3 to 14.2 ± 0.7 Ma These dates are complimentary to previous low temperature thermochronometer studies in the southern Ruby Mountains that surmise extension began approximately 17 – 15 Ma. These dates only incorporate low temperature thermochronometers meaning higher temperature thermochronometer systems should record older ages indicative of extension predating the late-Oligocene to early-Miocene ages acquired.

INTRODUCTION:

The Cenozoic lithospheric evolution of the western U.S. Cordillera is incompletely understood. Specifically, disagreement persists in the timing of the onset of significant extension and exhumation during either the late Cretaceous through the Eocene or mid- to late-Miocene. Evidence derived from analysis of mid- to deep-crustal rocks imply older (Cretaceous to Eocene) and more complex exhumational histories (Camilleri and Chamberlain, 1997; McGrew et al., 2000) while low temperature thermochronometry, fault gouge dating, and synextensional stratigraphic reconstruction suggests rapid, younger (Miocene), and less complex extensional unroofing (Colgan et al., 2010; Henry et al., 2011).

The Ruby Mountains in NE Nevada are an ideal area to address these controversies. Located within the Ruby Mountains is a large and continuous section of exposed, mid- to deep-crustal rocks exhumed by an Oligocene to early-Miocene extensional mylonitic shear zone (Figure 1). This metamorphic core complex provides a range of thermochronometers that document the exhumation history and rates within the region. Analysis of apatite and zircon (U-Th)/He thermochronology integrated with structural and field relations will document an exhumational history and help constrain the change from compression to extension in the region.

My research is part of a broader effort to determine when extension began and how fast it progressed in the Ruby Mountains – East Humboldt Range – Wood Hills Metamorphic Core Complex (REHW; Figure 1). The REHW is a Cordilleran metamorphic core complex with a brittlely extended cover of complexly faulted sedimentary rocks. The sedimentary units within the REHW superimpose a detachment fault and a broadly domiform exposure of mylonitic rocks that overprint a core of plutonic and high grade metamorphic rocks (Hudec 1992, McGrew et al., 2000). The evolution of the crustal geotherm and its relation to extension is critical to

understanding the lack of syntectonic stratigraphy that would accompany earlier phases of extension. The implications of these findings will be useful for public scientific outreach as we create interactive field trips, permanent and mobile displays, and learning modules and tutorials.

Reconstructing the tectonic and thermal evolution within the region will constrain the timing of processes that helped shape the western U.S. and provide a record of the movement of deep crustal rocks to the surface through the mid and upper crust. By determining the timing and length of exhumation, the evolution of the Cordillera may be analogous to regions such as the Andes, Himalayas, Alps, and Appalachian Mountains, thus providing insight into more fundamental tectonic processes.

GEOLOGIC SETTING:

Tectonic and Lithologic History of the REHW:

Rocks within the region range from Archean rocks to Holocene sediments (Figure 1). The western half of the REHW contains the highest grade portion of the complex, and is characterized by high-grade metamorphic and associated igneous rocks. The eastern portion, including the Wood Hills and Pequop Mountains, is primarily composed of lower-grade Paleozoic meta-sedimentary rocks with Cenozoic sedimentary and volcanic rocks. These Cenozoic units are also partially covered by late Cenozoic glacial, colluvial, alluvial fan, and active fluvial deposits (McGrew and Snoke 2015). The northern half of the East Humboldt Range exposes the deepest structural levels in the REHW.

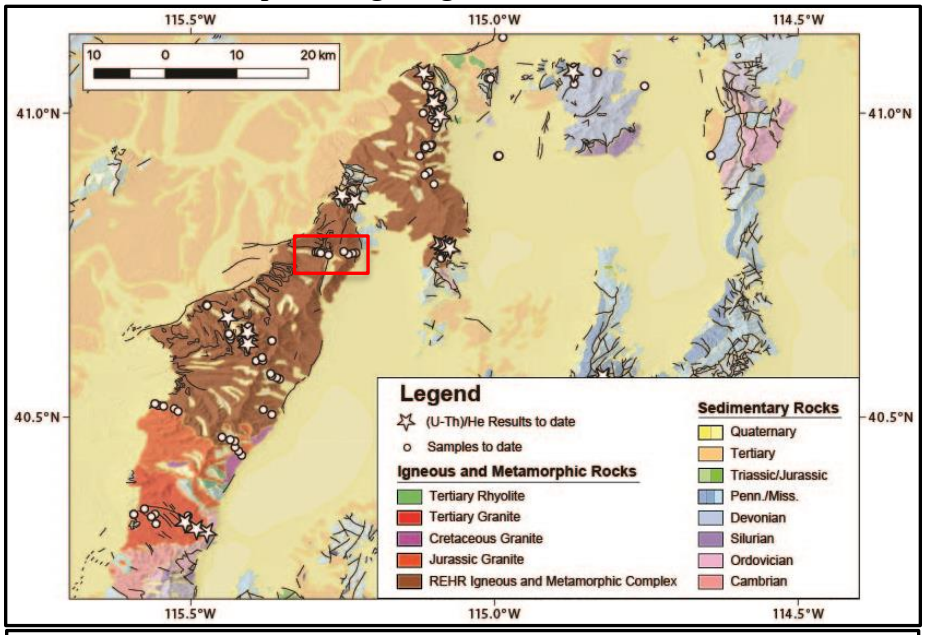

Figure 1. Geologic map of the REHW. The red box represents the 6 km transect and field mapping area of this study which spans Soldier Canyon and Kranka Creek (Metcalf 2019).

The Neoarchean to Paleoproterozoic Angel Lake gneiss complex contains both the deepest and the oldest rocks in Nevada including migmatitic biotite and biotite-sillimanite schist. Units of Cambrian to Neoproterozoic age units include metaconglomerates, metaquartzites, and a suite of metamorphic and leucogranitic rocks (Prospect Mountain and McCoy Creek Groups). Nonconformably overlying these units are a series of quartzites, marbles, carbonates, and dolomites ranging from Cambrian to Mississippian age, suggestive of a transition from a continental rift environment to that of a passive margin. Collectively, these units have been interpreted to represent a variably metamorphosed, Paleozoic passive margin sequence. Unmetamorphosed, Paleozoic sedimentary rocks containing steeply east-dipping strata, subdivided by steeply dipping faults (McGrew and Snoke 2015), deformed during the Antler orogenic event as the passive margin sedimentary lithologies were overlain by the conglomeratic Diamond Peak Formation. Succeeding the Diamond Peak Formation is a host of passive margin sedimentary sequences lasting through the Permian.

The Mesozoic is represented by amphibolite facies metamorphism and two-mica granite emplacement, suggestive of major crustal shortening and thickening in a back-arc setting behind the Sierran-Klamath-Blue Mountains arc (Hudec 1992). Mid-Cretaceous to Paleogene leucogranites and accompanying Barrovian metamorphism indicate maximum temperatures ≤ 800°C and pressures ≤ 10 kbar (Figure 2; McGrew

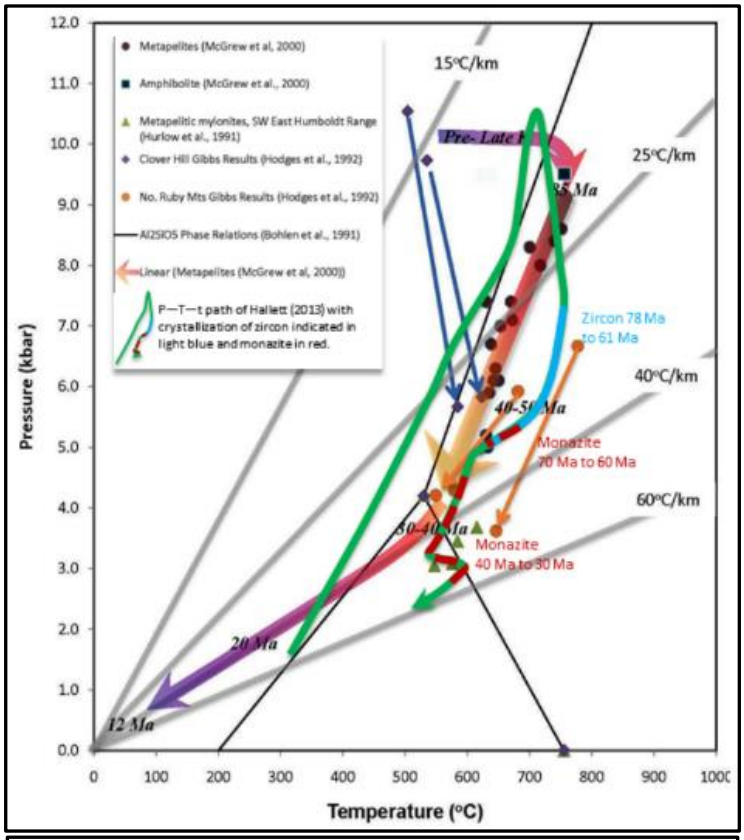

Figure 2. Diagram summarizing P-T-t results from the REHW (Hurlow et al., 1991; Hodges et al., 1992; Hallett and Spear, 2013; McGrew et al.,

et al., 2000; Hallett and Spear 2014; Wills 2014). These temperature and pressure conditions were followed by decompression of ~2 – 4 kbar by the late Cretaceous (Hallett and Spear 2014). Multiple thrust faults and folds throughout the region date to this time period (Howard 1980; McGrew and Snoke 2015), characteristic of the Sevier orogeny. The mid- to late-Cretaceous was a time of significant crustal shortening, thickening, and accompanying metamorphism and magmatism.

The Miocene contains basaltic and rhyolitic dikes cutting through varying different conglomeratic and terrestrial sedimentary formations. Of note, the early Miocene contains calcareous sandstone and fine-grained lacustrine limestone in the sedimentary sequence of the Clover Creek Formation while the upper portion is primarily conglomerate containing Paleozoic lithologies. Nonconformably superimposed over the Clover Creek Formation, the Humboldt Formation forms a sharp contact and is defined by the abundance of volcaniclastic debris and terrestrial sediments. The Humboldt Formation and subsequent sedimentary rocks form a stratigraphic layer ~ $\leq$ 6 km.

Due to its immense size, the Humboldt Formation may be divided into two components separated by the Willow Creek rhyolite suite. The section of the Humboldt Formation directly overlying the Clover Creek Formation is composed of tuffaceous siltstone, siliceous siltstone, and very fine-grained sandstone with volcaniclastic pebble conglomerate and very coarse-grained sandstone comprising much of the unit, with some vitric ash. The Willow Creek rhyolite suite separates the second designation of the Humboldt Formation and yields an age of 14.8 to 13.4 Ma from sanidine K-Ar dating (Snoke et al., 1997). The Humboldt Formation superseding the Willow Creek rhyolite suite is characterized by tuffaceous sandstone and siltstone, polymictic conglomerate, lacustrine limestone, accretionary lapilli tuff, and vitric ash. Overall, the

Humboldt Formation represents significant erosion and deposition within sedimentary basins, characteristic of syntectonic sediments.

A gently west-dipping, >1 km thick, normal-sense mylonitic shear zone exhumed the REHW for > 150 km along strike, causing significant decompression and rapid cooling (McGrew et al., 2000); however, the onset of this faulting, and how deep crustal exhumation relates to surface faulting, has yet to be agreed upon. The late-Miocene is categorized by high-angle normal faulting associated with the extension of the Basin and Range.

Historic Thermochronology and Thermobarometry:

The integration of thermobarometry and thermochronology in the high grade metamorphic core provides a constraint to the higher temperature of the P-T-t path. U-Pb geochronometry of zircons constrain the crystallization age of a granitic dike in the Pequop Mountains resulted to be 154 ± 5 Ma (Figure 3A; Camilleri and Chamberlain, 1997). This age provides an upper limit to the onset of metamorphism during the Sevier orogeny in the REHW. Peak metamorphic conditions in the Pequops are constrained by a sphene $^{207}Pb/^{206}Pb$ age of 84.1 ± 0.2 Ma, interpreted to be coeval with biotite-garnet thermometry, indicating maximum temperatures between ~400 – 475°C (Camilleri and Chamberlain, 1997). Muscovite $^{40}Ar/^{39}Ar$ thermochronology reflects a cooling through ~450°C at 75 Ma (Thorman and Snee, 1988). Therefore, combined U-Pb and $^{40}Ar/^{39}Ar$ data from the Pequop Mountains

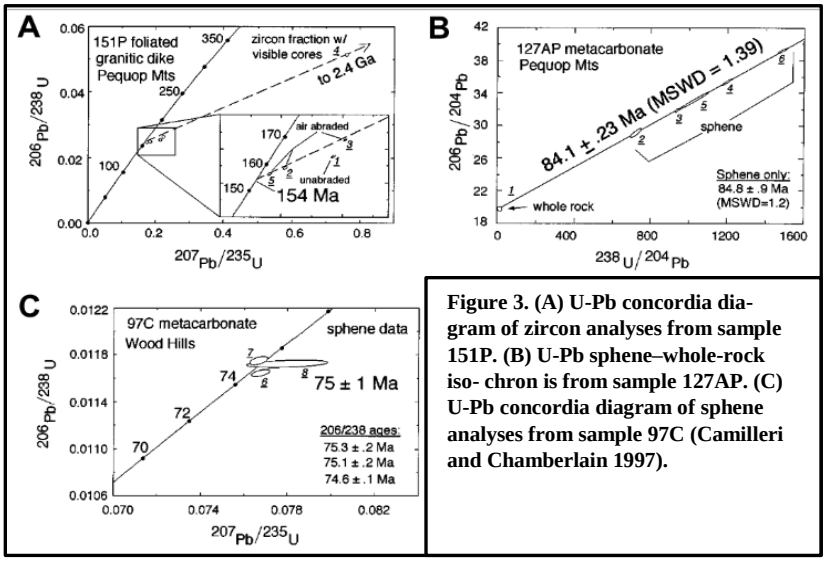

Figure 3. (A) U-Pb concordia diagram of zircon analyses from sample 151P. (B) U-Pb sphene–whole-rock iso- chron is from sample 127AP. (C) U-Pb concordia diagram of sphene analyses from sample 97C (Camilleri and Chamberlain 1997).

yield a temperature-time curve with a metamorphic peak of ~425 – 475°C at 84.1 ± 0.2 Ma followed by rapid cooling through ~450°C at 75 Ma (Figure 3B).

Similarly, a temperature time path for the Wood Hills was constructed using the same methods. $^{40}Ar/^{39}Ar$ data from biotite and muscovite indicate cooling through ~300 °C between 56 and 47 Ma (Thorman and Snee, 1988). The sphene data plot from $^{207}Pb/^{206}Pb$ isochron indicates a date of 75 ± 1.0 Ma (Figure 3C) with an interpreted cooling temperature of 580°C. Combined U-Pb and $^{40}Ar/^{39}Ar$ data for the Wood Hills yield a temperature-time curve that documents cooling through ~580 °C at 75 Ma followed by cooling through ~300 °C at 56 – 47 Ma (Camilleri and Chamberlain, 1997). Synthesized cooling-age dates from both the Pequops and Wood Hills yield 14 – 19 and 13 – 15 °C/Myr, for shallow and intermediate structural levels, from the late Cretaceous to Tertiary (Camilleri and Chamberlain, 1997).

Hornblende cooling ages for the Wood Hills record 36 Ma at shallower levels to 29 Ma at deeper structural levels while biotite, muscovite, and potassium feldspar $^{40}Ar/^{39}Ar$ data possess cooling ages of 27 to 21 Ma (McGrew and Snee 1994). Such age relations of >7 Myr suggest gradual cooling from higher temperatures, and when combined with AFT ages, are plausible if the REHW detachment fault dipped >30° between 300 – 100°C isotherms (McGrew and Snee 1994). McGrew and Snee (1994) note initial unroofing in the Wood Hills coincides temporally with the cessation of thrusting in the late Mesozoic to early Tertiary. McGrew and Snee (1994) continue to state gravitational collapse of tectonically thickened crust in the internal zone of the Sevier belt could have driven initial exhumation and unroofing.

McGrew et al. (2000) found similar age relationships from $^{207}Pb/^{206}Pb$ dates of zircon in leucogranites from the Lizzies Basin block in the East Humboldt Range, yielding an age of 84.8 ± 2.8 Ma. Thermobarometric results show an elongate data spread nearly parallel to the

kyanite=sillimanite point, from > 9 kbar and 800°C to ~5 kbar and 630°C (McGrew et al., 2000). This cooling, from Late Cretaceous to Oligocene, yields a decompressional cooling trajectory of ~40°C/kbar, implying unroofing outpaced cooling due to the steepness of the P-T-t path. $^{40}Ar/^{39}Ar$ hornblende data from the northern Ruby Mountains record cooling ages of 26 to 32 Ma at 550 – 650 °C during Oligocene mylonitization, placing a lower bracket on the age of rim equilibration (Dallmeyer et al., 1986). Combining the P-T data with $^{40}Ar/^{39}Ar$ hornblende cooling ages implies that > 2.5 kbar of decompression probably occurred before the mid-Eocene (McGrew et al., 2000).

Other heating, exhumation, and cooling rates have also been measured based on petrologic relationships in both the Winchell Lake nappe and the Lizzies Basin block. Timing of monazite growth, representing greenschist facies metamorphism below the garnet isograd, with zircon ages from the same samples, interpreted to represent crystallization of melt formed in situ, suggest as much as 7 kbar of compression followed by ~3 – 4 kbar of decompression occurred between these accessory mineral growth events, coupled with ~200°C of heating and ~60°C of subsequent cooling (Hallett and Spear 2014). Petrologic relationships indicate the Lizzies Basin block experienced ~3 kbar of compression and ~300°C of heating, followed by 2 – 3 kbar of decompression and ~200 °C of cooling prior to exhumation of the metamorphic core complex (Hallett and Spear 2014).

Within the southern Rubies, Miocene sedimentary rocks, located within the hanging wall of the fault system, are 11.6 to 15.2 Ma in age. AFT data from Jurassic plutons east and west of the southern Rubies suggest near-surface temperatures (<60 °C) since the Cretaceous. Similar to McGrew and Snee (1994), Colgan et al. (2010) report biotite $^{40}Ar/^{39}Ar$ ages range at shallow and deeper depths from 33 to 30 Ma and 25 to 24 Ma, respectively. Additionally, AFT ages from a

transect across the Harrison Pass Pluton record ages between 25 to 12 Ma with Apatite (U-Th)/He ages with a weighted mean of 14.4 ± 0.6 Ma (Colgan et al., 2010). Modeled t-T paths record rapid cooling from >120 °C to <40 °C from 17 to 15 Ma (Colgan et al., 2010).

SAMPLES, METHODS, RESULTS:

Samples:

My focus area spans a 6 km East-West transect from Kranka Creek on the East flank of the Ruby Mountains to the entrance of Soldier Canyon on the West flank. The East flank is steep, representative of recent high angle reverse faulting, and consists of multi-deformed, upper amphibolite facies, migmatitic rocks. The West flank is gently dipping and contains a mylonitic shear zone >1 km thick with a West-Northwest shear sense from observed lineations. Within this region, I collected 11 samples from 8 sites consisting primarily of monzogranites and leucogranites derived from Cambrian, Ordovician, and Devonian age sedimentary protoliths. Leucogranites in the region are primarily late-Cretaceous in age, 85 ± 3 Ma (Snoke et al., 1990; McGrew et al., 2000); however, a relatively small proportion of leucogranitic rocks are observed cutting or intermingled with 40 Ma quartz diorite and 29 ± 0.5 Ma biotite monzogranites (Wright and Snoke, 1993).

Located within the field area of the Northern Ruby Mountains, the image below is looking eastward, down Kranka Creek.

RGD18-13: Foliated, mylonitized granite. Well foliated layers intermingling with marble, rare quartzite. RGD18-13A is a foliated granite. RGD18-13B contains biotite and sphene. Observed sphene forms mm thick layers within the biotite (Figure 4).

Figure 4. RGD18-13

RGD18-14: High biotite content, plagioclase feldspar, potassium feldspar, and quartz are present within a medium grained (<1 mm), massive, biotite monzogranite or biotite granodiorite. Sample possesses a whiteish, light grey coloration with black pepper action from biotite. RGD18-14A contains a mafic intrusion and is located within a quartzite/marble sedimentary package (Figures 5, 6).

Figure 5. RGD18-14A

Figure 6. RGD18-14B

RGD18-15: High biotite content, plagioclase feldspar, garnet, and sphene are present within a mafic, granodoiritic mylonite (Figure 7). Foliation and large phenocrysts are abundant. The outcrop is glacially polished and located beneath a cliff of mylonites and highly deformed marbles with a 3 ft. thick vertical shear component. Sample appears migmatitic in some places (Figure 8).

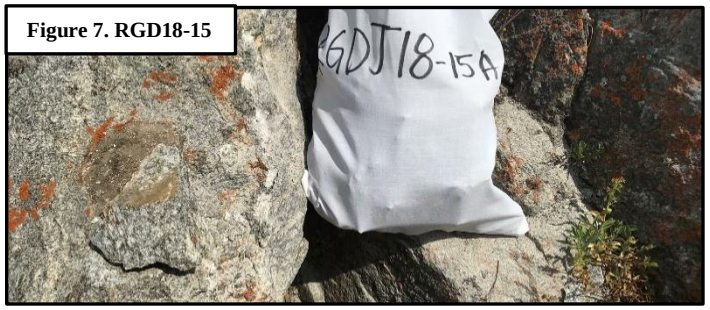

Figure 7. RGD18-15

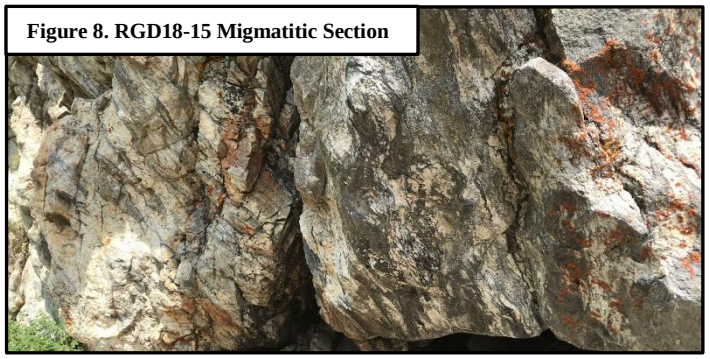
Figure 8. RGD18-15 Migmatitic Section

RGD18-16: Garnet-bearing, marble mylonites are co-located with a felsic pegmatitic layer and a fine grained granodiorite layer ~3 ft. thick. The pegmatitic layer has large potassium feldspar phenocrysts, biotite, muscovite, and garnet. Foliation is present throughout the sample as well as a mafic layer. RGD18-16A is the felsic, pegmatitic, garnet bearing unit (Figure 9). RGD18-16B is the fine grained, granodioritic mylonite (Figure 10). Fine grained layer possesses garnets, ≤ 0.5 mm in diameter, and biotite.

Figure 9. RGD18-16A

Figure 10. RGD18-16B

RGD18-17: Quartzite, hornblende, biotite, garnet, and mm-sized zircons are present within a monzodioritic quartz diorite (RGD18-17A, Figure 11). RGD18-17B contains more mafic intrusions within a quartzite (McCoy Creek Group).

Figure 11. RGD18-17

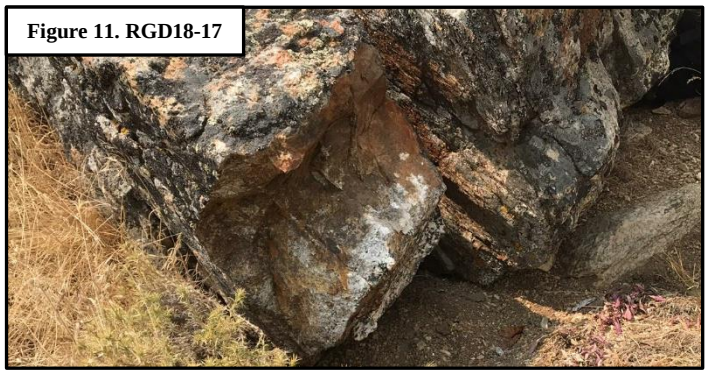

RGD18-18: Abundant potassium feldspar and quartz leucogranites are contained within foliated and lineated biotite quartzites (McCoy Creek Group, Figure 12).

Figure 12. RGD18-18

RGD18-19: Large outcrops of course grained monzogranite are collocated with thin layers of dirty quartzite (McCoy Creek Group). Within this outcrop is a mafic boudain, folds, and slickensides. Well defined foliation is visible in both the quartz and biotite (Figure 13).

Figure 13. RGD18-19

RGD18-20: Plagioclase feldspar, hornblende, and titanite comprise a mafic diorite (Figure 14).

Figure 14. RGD18-20

Methods Background:

Apatite and zircon (U-Th)/He thermochronometry are important tools for quantifying the cooling history of rocks as they pass through the upper 1 – 7 km of the crust (Ehlers and Farley, 2003, Guenthner et al., 2013). Applications of apatite and zircon (U-Th)/He thermochronology primarily include determination of uplift, exhumation, and landscape formation. Radiometric dating of apatite and zircon measures the ratio of decayed parent atoms, primarily ^{238}U, ^{235}U, and ^{232}Th to ^{206}Pb, ^{207}Pb, ^{208}Pb respectively along with a minor contribution from ^{147}Sm, and daughter product, ^{4}He, formed from the α decay of said parent atoms.

Thermochronology involves systems in which the transition from daughter product, ^{4}He, diffusing through the crystal lattice and escaping the system, open behavior, to complete retention of the daughter product within the crystal, closed system behavior, is thermally controlled. This transition typically occurs over a relatively narrow temperature range, referred to as the closure (or blocking) temperature. Therefore, any dates derived from analysis of apatite or

zircon He data are not necessarily representative of the date at which a mineral crystallized but of the integrated thermal history since the onset of radiation damage accumulation and He retention. Because a system may transition from open to closed behavior, and vice versa, multiple times throughout a crystal's life, the date measured records the last thermal event experienced; thus, in order for a mineral to be a desirable thermochronometer, it must contain abundant parent atoms, possess low initial daughter products within the decay series, and its transition must be dominantly controlled by temperature.

Apatite possesses a closure temperature of ~70°C. However, as the apatite (U-Th)/He thermochronometer approaches its closure temperature, it is characterized by a partial retention zone (PRZ). The PRZ is a temperature range, between ~40 – 80°C, over which He is neither entirely retained nor lost by diffusion (Wolf et al., 1998). Within the PRZ, He will be retained by 90 to 10% of its production and will achieve production and loss equivalence within this range based on isothermal holding conditions. Additionally, the amount of accumulated radiation damage in a crystal affects the temperature range of the PRZ (Flowers et al., 2009; Guenthner et al., 2013). Apatites with lower eU (effective uranium: a proxy for radiation damage, eU = U + 0.235 X Th) and less radiation damage have lower He retentivity than those with higher eU and greater radiation damage; therefore, the PRZ plots at higher temperatures with increasing eU (Figure 15).

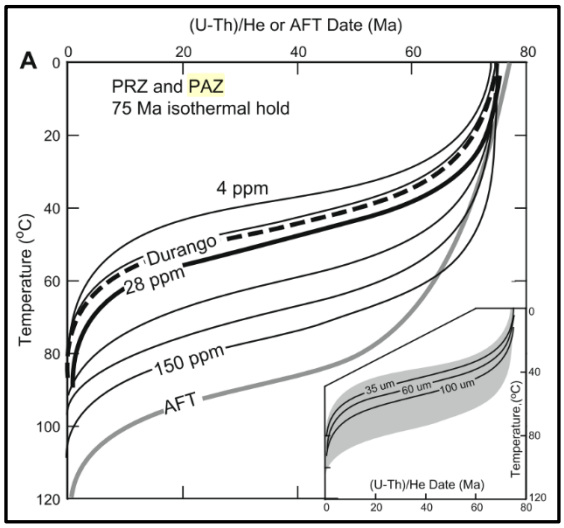

Figure 15. PRZ for apatites characterized by eU values from 4 to 150 ppm (Flowers et al., 2009).

Zircon (U-Th)/He thermochronometer temperature sensitivity is also dependent on the amount of accumulated radiation damage. As U and Th decay, the resultant radiation damage disrupts He diffusion pathways, thus decreasing He diffusivity, and raising the closure temperature (Guenthner et al., 2013). However, with very high levels of accumulated damage, damage zones become interconnected and lead to a dramatic increase in He diffusivity and lowering of the closure temperature (Figure 16). At higher temperatures, a crystal is able to revert itself to a more energetically favorable state by annealing radiation damage; if a crystal becomes cool enough and reaches its closure temperature, radiation damage will accumulate. Therefore, the temperature sensitivity of zircon He dates depends upon both the amount of U and Th decay and the amount of annealing that has occurred. The closure temperature of the crystal can be estimated based on the accumulated α dose (Figure 16).

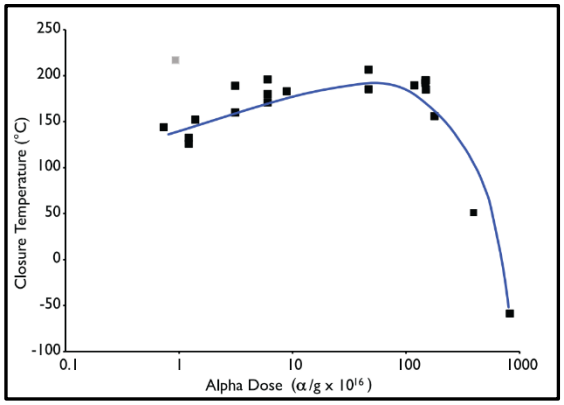

Figure 16. Plot of closure temperature vs. α dose for zircon (U-Th)/He thermochronology. Closure temperatures were calculated using a spherical geometry, diffusion domain size of 60 microns, and cooling rate of 10 °C/Myr (Guenthner et al., 2013).

Methods:

Apatite grains were analyzed at the University of Colorado Thermochronology Research and Instrumentation Laboratory (TRaIL). Rock samples were crushed, pulverized, and run through hydrodynamic, heavy liquid, and magnetic separation steps to obtain pure mineral separates. Mineral grains were handpicked using a Leica M165 binocular microscope. Grains were selected for quality based upon the following criteria: crystal size > 60 μm, euhedral, and, regarding apatites, lack of inclusions. Upon packing mineral grains into individual Nb tubes, the Nb packets were loaded into an ASI Alphachron He extraction and measurement line. The packets were placed in a UHV extraction line (~$3x10^{-8}$ torr) and heated with a 25W diode laser to

~800 – 1100°C for 5 to 10 minutes to extract the radiogenic ^{4}He. Degassed apatite grains were then dissolved with a ^{235}U – ^{230}Th – ^{145}Nd tracer in HNO3 and baked at 80°C for 2 hours.

Zircons were dissolved via multiple acid-vapor dissolutions. Grains were spiked with a ^{235}U - ^{230}Th - ^{145}Nd tracer, mixed with Optima grade HF, placed in a Parr dissolution vessel, and baked at 220°C for 72 hours. After removal, the grains were dried on a hot plate and were subject to a second round of acid-vapor dissolution, 6N Optima grade HCl was added and the grains were baked at 200°C for 24 hours. Afterwards, vials were again dried via a hot plate. A 7:1 HNO3:HF mixture was then added to each vial and cooked at 90°C for 4 hours. Once dissolved, both sample zircons and apatites, as well as standards consisting of Fish Canyon Tuff zircons and Durango fluorapatites, were analyzed via ICP-MS for U, Th, and Sm content using an Agilent 7900 quadrupole ICP-MS. Upon acquisition of measured U, Th, and Sm, He dates were calculated based on the methods in Ketcham et al. (2011). The natural occurring ^{238}U/^{235}U ratio used in data reduction is 137.818 per Hiess et al. (2012). All resultant data are within one standard deviation (σ) of the mean except for analytical uncertainty of acquired dates (2σ).

The production of ^{4}He, α particles, is a function of the decay series of ^{238}U, ^{235}U, and ^{232}Th and is represented by the following ingrowth equation:

$$He = 8\ ^{238}U\ (e^{\lambda_{238}t} - 1) + 7\ (^{238}U/137.818)\ (e^{\lambda_{235}t} - 1) + 6\ ^{232}Th\ (e^{\lambda_{232}t} - 1) + ^{147}Sm\ (e^{\lambda_{147}t} - 1)$$

where He, U, Th, and Sm refer to present day amounts, t is the accumulation time or He age, and λ is the respective decay constant ($\lambda_{238} = 1.551 \times 10^{-10}$ yr^{-1}, $\lambda_{235} = 9.849 \times 10^{-10}$ yr^{-1}, $\lambda_{232} = 4.948 \times 10^{-11}$ yr^{-1}, $\lambda_{147} = 6.54 \times 10^{-12}$ yr^{-1}; Farley 2002). Coefficients preceding U and Th abundance account for the varying α particles produced in each respective decay series while the 1/137.818

ratio of $^{235}U/^{238}U$ accounts for the present day ratio. Of note, inserting an age into the age equation for t and solving for He results in the α dose of a zircon crystal. This is how α -dose estimates, used later in this study, were calculated.

Upon α decay of ^{238}U, ^{235}U, ^{232}Th, and ^{147}Sm, the α particles (^{4}He atoms) travel ~20 μm away from their parent nuclides. This means that He has the potential to be expelled from the crystal for parent atoms sitting within ~20 μm of the crystal's boundaries. Therefore, any dates acquired must be corrected for this non-diffusive loss of He using an α retention factor. Within our calculations, we assume a homogenous distribution of U and Th within our samples to correct for α ejection. This α ejection correction is geometric and thus dependent on both the crystal's shape and size. Unfortunately, U and Th zonation may not be uniform and instead be either highly concentrated in cores or around the rim of a crystal, respectively leading to greater retention and a younger date or less retention and an older date than reported. Parent isotope zonation, which we did not characterize for this study, can therefore cause dispersion in (U-Th)/He dates.

Final uncertainties reported with our dates only incorporate measurement uncertainties in total U, Th, Sm, and He amounts. However as mentioned above, corrections for α ejection assume a uniform U and Th distribution which may not be the case. Therefore these uncertainties may affect our ejection corrections, but for practical analytical reasons are not addressed here.

Additionally, mass calculations, required to determine U, Th, Sm, and He as well as eU concentrations, and α ejection corrections are based upon ideal crystal geometries which may be oversimplifications. These uncertainties are currently difficult to constrain and consequently are not included in our final date uncertainties. As a result, the interpretations of our findings focus on observed large scale trends within our data.

Results:

RGD18-15 was the only mineral separate to yield desirable, non-included apatite grains. Out of the five apatite grains analyzed from RGD18-15, three grains possessed high Re values (the Re% value for RGD18-15_a5 is reported as 99.9 due to rounding errors, Table 1). Upon further analysis, we concluded these high Re values are indicative of micro-inclusions most likely undetected during initial inspection of the selected grains. Apatite He dates recovered from analyzed grains are mid-Miocene in age. RGD18-15_a2 and a4 respectively yield dates of 18.5 ± 1.3 and 14.2 ± 0.7 Ma, providing a mean age of 16.3 ± 1.0 Ma (Figure 17A).

Figure 17A RGD18-15

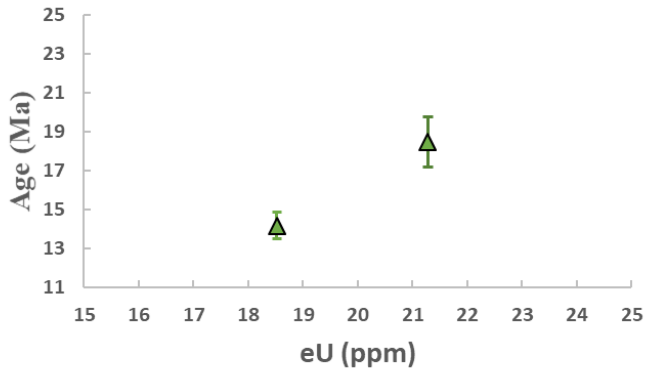

Figure 18A

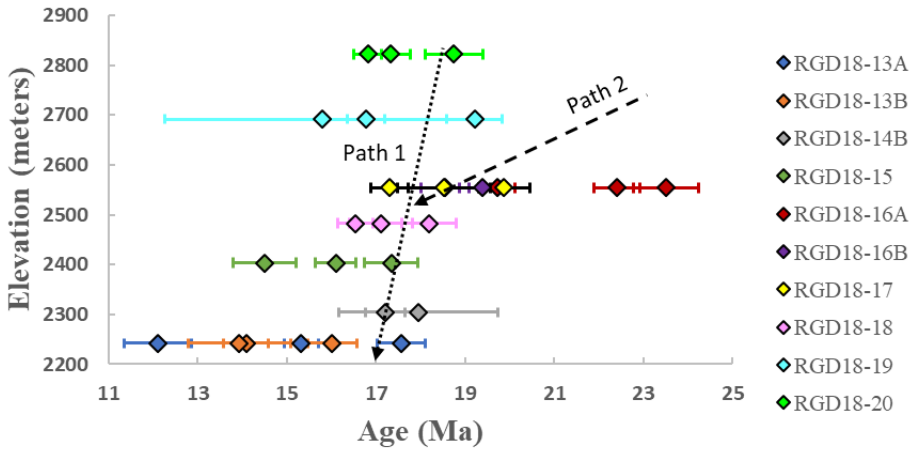

Figure 18B

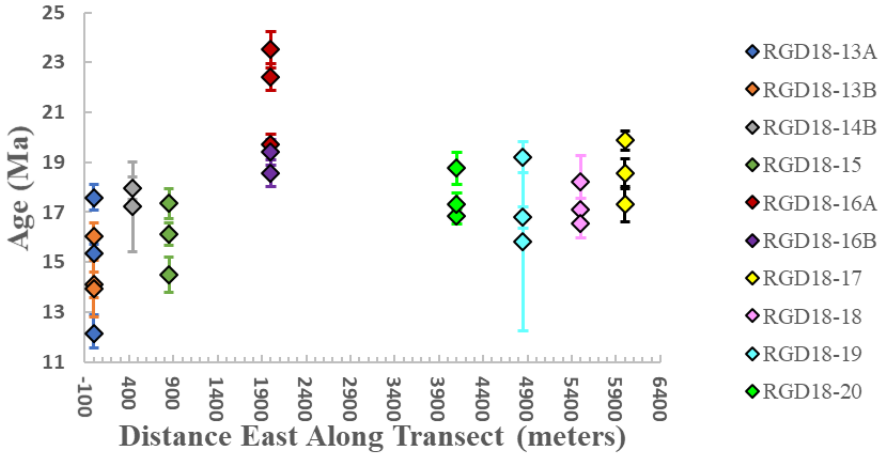

Elevation vs. age, transect distance (which is approximately parallel to transport direction) vs. age, and eU vs. age profiles of zircon He dates all depict broadly positive trends, with exception of RGD18-16 (Figures 18A, B, C).

Figure 18C

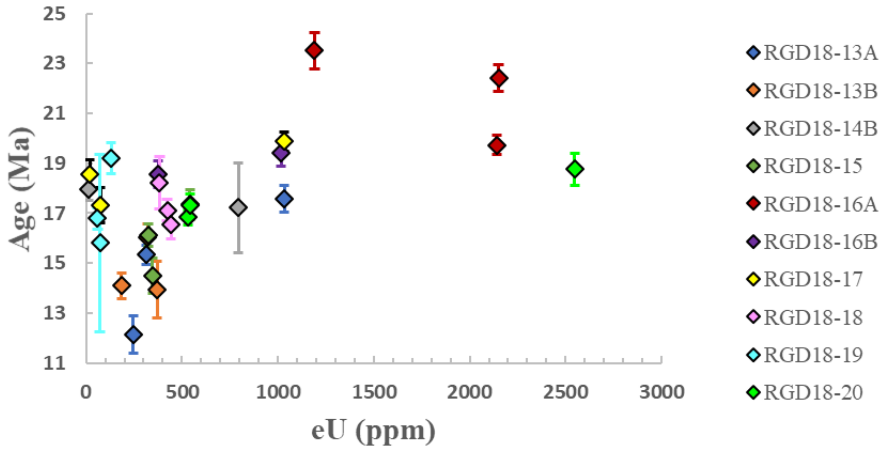

Zircon He dates show an age elevation trend with RGD18-13A and RGD18-13B, the lowest elevation samples at 2242 m, possessing the youngest mean age of 14.8 ± 0.7 Ma while RDG18-16, the highest elevation sample on the West flank at 2554 m, has the oldest mean age of 20.7 ± 0.5 Ma. The highest elevation sample in the transect is RGD18-20 at 2822 m, located along the ridge of the northern Ruby Mountains, with a mean age of 17.6 ± 0.5 Ma. Fitting a cooling exhumation history path to the age vs. elevation plots results in two plausible scenarios. Path 1 shows an exhumational history in which onset of exhumation was rapid and contained within a singular event. Path 2 represents an exhumational history in which exhumation on the fault was more gradual until ~18 Ma, resulting in a faster event via Path 1.

Measured eU concentrations show a positive trend across all samples and exhibit a positive correlation between age and eU (Figures 18C, 19A – 26A). Relationships between age and grain size are less consistent with the majority of samples possessing positive correlations while RGD18-14 and RGD18-17 display negative trends (Figures 19B – 26B). The majority of sampled zircons exhibit eU concentrations less than 550 ppm with a few outliers: RGD18-13A_z01, eU of 1030 ppm, and RGD18-14B_z05, eU of 795 ppm (Figures 19A, 20A). Additionally, two samples demonstrate comparatively high eU concentrations. RGD18-20 contains eU concentrations of 533, 541, and 2548 ppm while RGD18-16 contains grains with eU concentrations of 1017, 1191, 2140, and 2150 ppm (Figures 26A, 22A).

Figure 19A RGD18-13

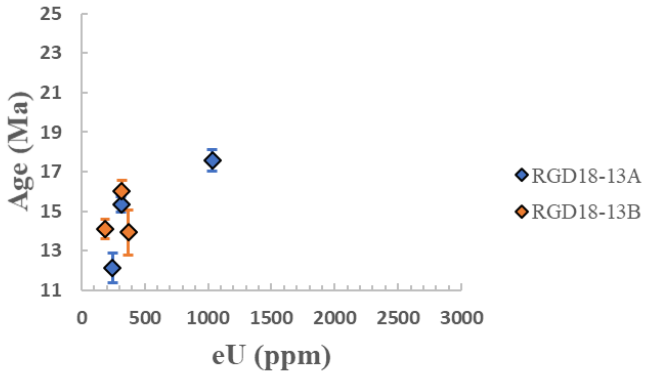

Figure 19B RGD18-13

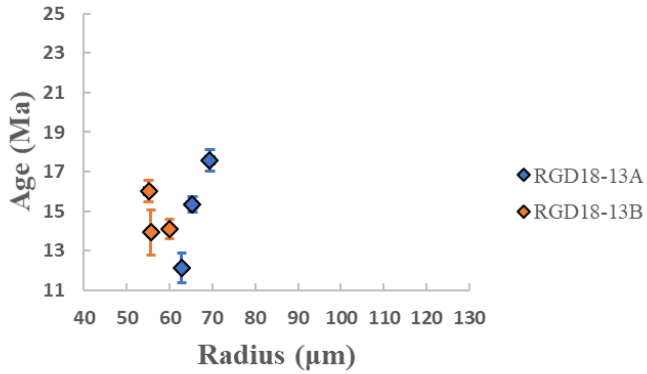

Figure 20A RGD18-14

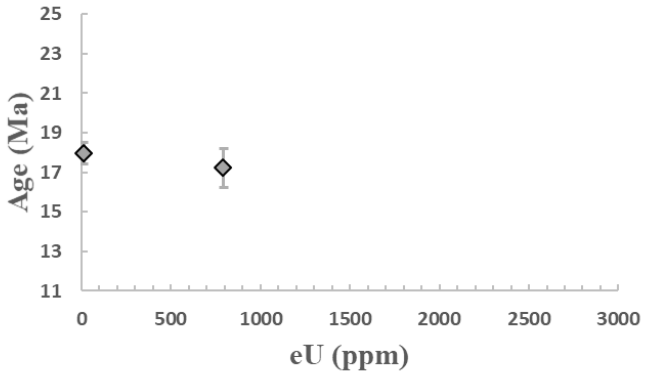

Figure 20B RGD18-14

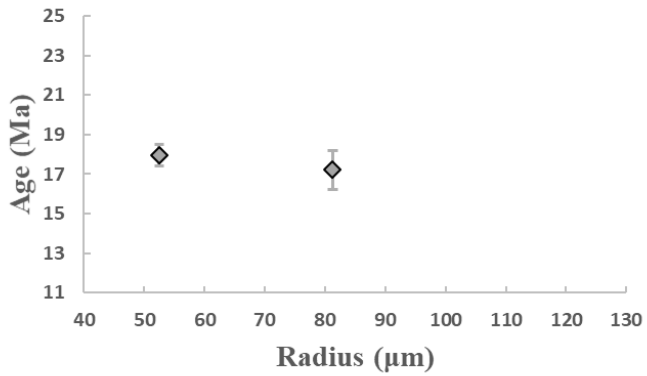

Figure 21A RGD18-15

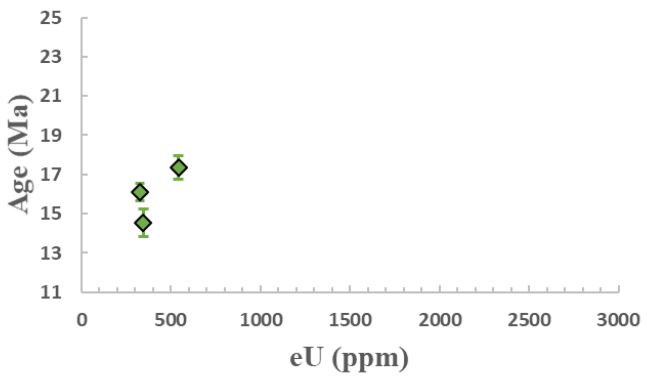

Figure 21B RGD18-15

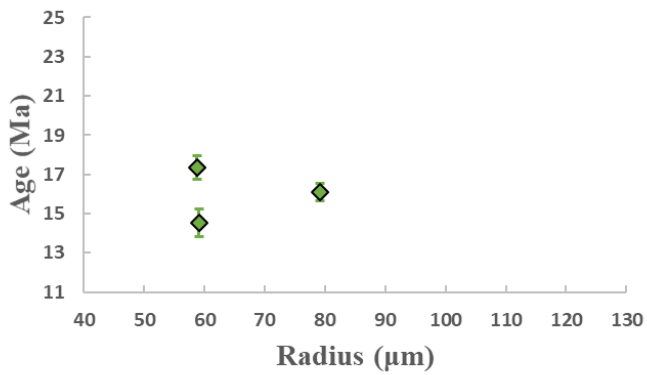

Figure 22A RGD18-16

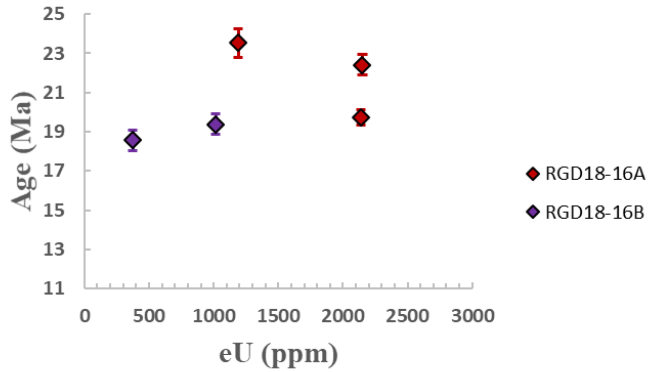

Figure 22A RGD18-16

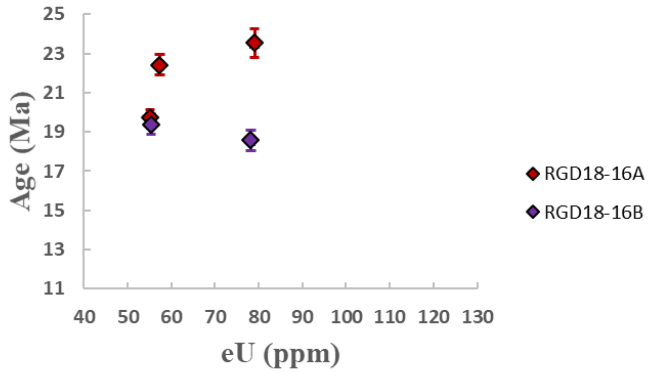

Figure 23A RGD18-17

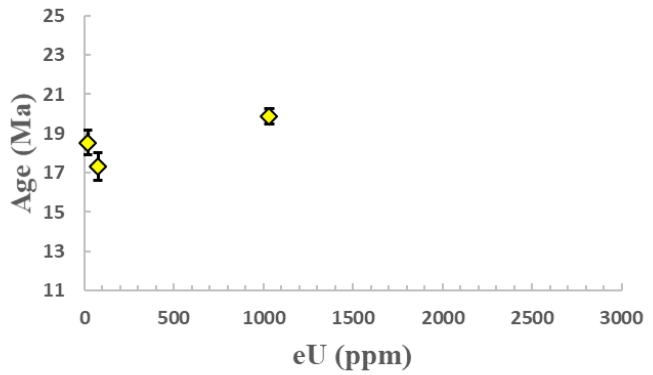

Figure 23B RGD18-17

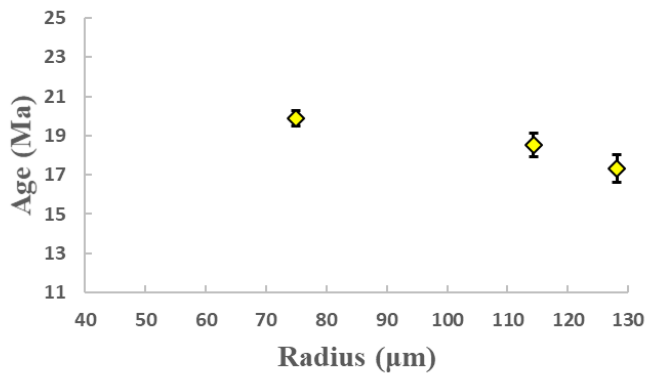

Figure 24A RGD18-18

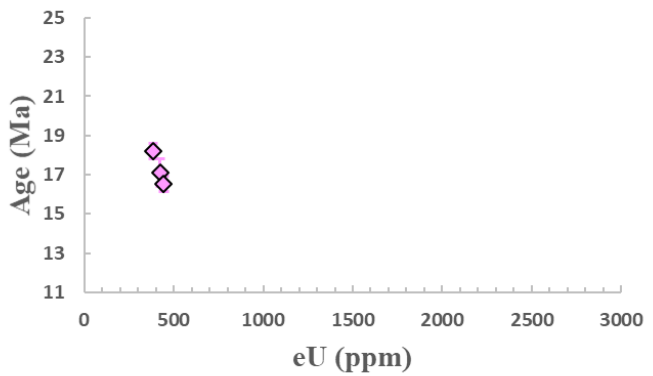

Figure 24B RGD18-18

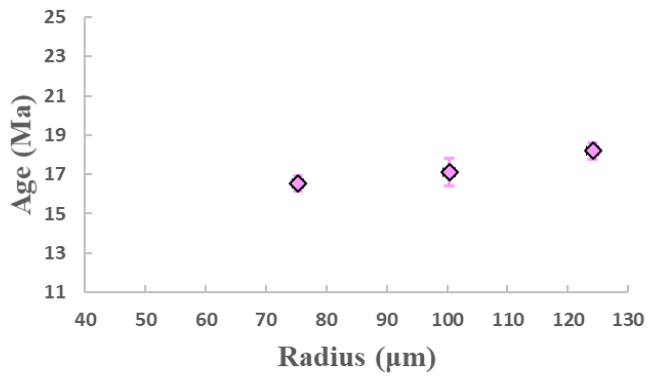

Figure 25A RGD18-19

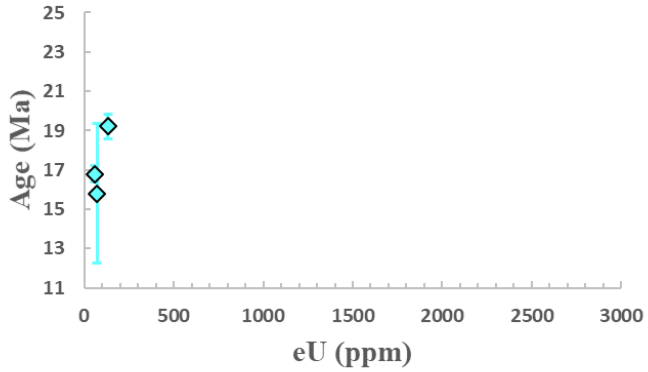

Figure 25B RGD18-19

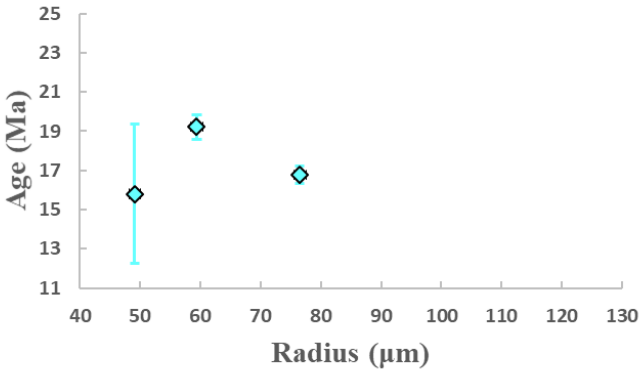

Figure 26A RGD18-20

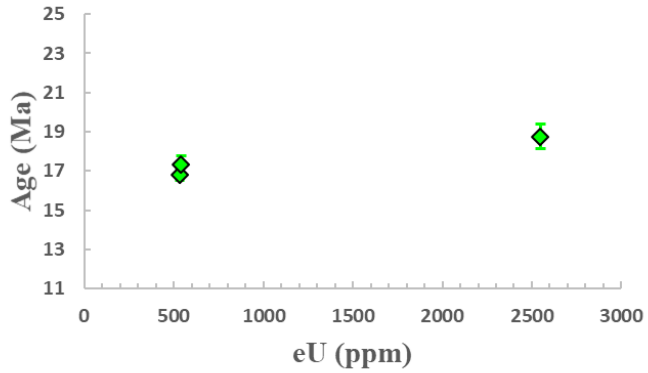

Figure 26B RGD18-20

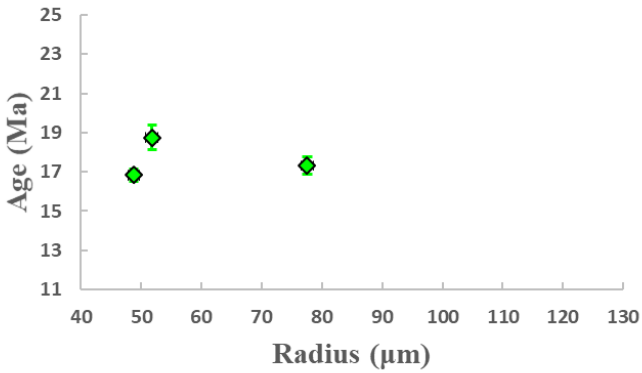

DISCUSSION:

Variations and range of ages may be due to several factors including grain size, accumulated radiation damage (eU), and U and/or Th zoning. The total accumulation of radiation damage (represented by eU concentrations) may result in both positive and negative eU vs age plots, depending on the total amount of accumulated radiation damage. Assuming similar thermal histories, grains with lower eU concentrations are indicative of losing a greater portion of their He, resulting in a younger age date while grains with greater radiation damage are able to retain more He and provide an older age date (Guenthner et al., 2013). Additionally, the size of the grains is important when considering the retention of He within the system because He takes longer to diffuse out of larger grains. In addition, these dates assume a uniform U and Th distribution in the crystals, which may not be the case.

Accumulation of radiation damage by U and Th α decay as well as the amount of U and Th within our analyzed zircons provides an α dose range of 1 – 3 α/g X 10^{16} with an accumulation time of ~17 Myr (Figure 18A). This α dose range correlates to a closure temperature range of 145 – 160℃ based on Guenthner et al. (2013) (Figure 16). Thus, between 14.8 ± 0.7 to 20.7 ± 0.5 Ma zircon crystals were cooling through a temperature gradient of 145 – 160℃ .

The eastern flank of the Rubies is a normal fault associated with extension during the mid-Miocene. As slip on the fault propagated westward, samples deepest within the crust, RGD18-19 to RGD18-17, experienced the greatest exhumation, while samples in the down-dip direction of the fault trend systematically younger (Stockli 2005, Figure 27). Of note, RGD18-16 represents the oldest age acquired with an average age of 20.7 ± 0.5 Ma. This discrepancy in the

trend of progressively older dates eastward along the transect may be due to the high eU concentrations within these grains and signify greater radiation damage. Omitting RGD18-16, the oldest date at the eastern most section of the transect, RGD18-17, and youngest date on the western start of the transect, RGD18-13, are consistent with this normal fault system.

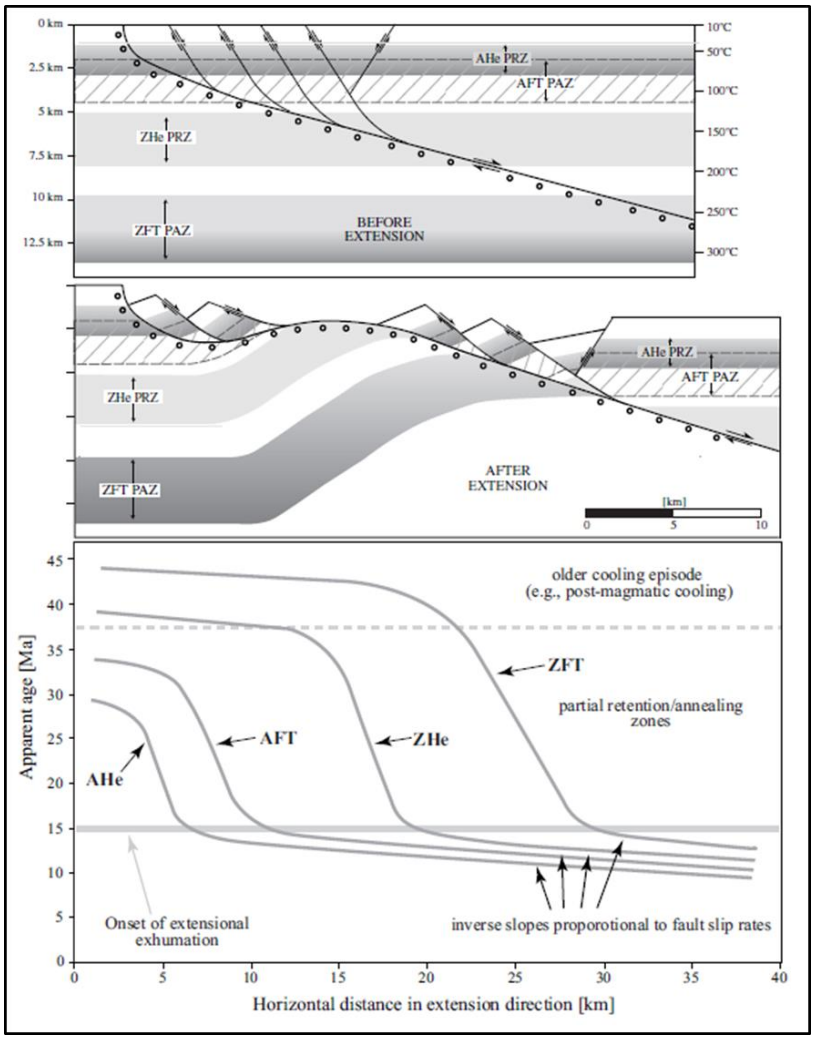

Figure 27. Structural evolution and exhumation of footwall rocks from beneath low-angle normal faults (Stockli et al., 2005).

Due to high Re% values, we chose to exclude acquired ages from RGD18-15_a1, a2, and a3. The remaining ages consist of 18.5 ± 1.3 and 14.2 ± 0.7 Ma, from RGD18-15_a2 and a4 respectively. These dates correspond to the apatite cooling through a closure temperature range of 60 – 70°C (Figure 15; Flowers et al., 2009).

Combining our closure temperature range of 145 – 160°C and age range of 14.8 ± 0.7 to 20.7 ± 0.5 Ma for our analyzed zircon grains with our apatite closure temperature range of 60 – 70°C and age range of 18.5 ± 1.3 and 14.2 ± 0.7 Ma implies both the zircon and apatite systems passed through their closure temperatures and began retention of He around ~17 Ma. Said movement from one temperature gradient to another over such a short time span, or concurrently, is indicative of significant and rapid exhumation as illustrated by Path 1 (Figure 18A).

The findings within Colgan et al. (2010) interpret rapid Miocene slip on the Ruby detachment to have begun between 16 and 17 Ma. This is founded upon the oldest dated Miocene basin fill in the study area and nearby as well as within uncertainty of all apatite fission track and (U-Th)/He ages. Additionally, the study only supports cooling through the apatite fission track and He systems from 120 – 60°C between 16 – 14 Ma. Relatedly, Henry et al. (2011) supports rapid mid-Miocene cooling through near surface temperatures of 120 – 40°C between 17 – 16 Ma. However, our inclusion of zircon (U-Th)/He temperatures and ages demonstrate more substantial cooling during this time from 160 – 60°C. Assuming geologically reasonable geothermal gradients, this implies an additional 3.5 – 6.6 km of exhumation during this time period, suggesting greater exhumational processes throughout the northern Ruby Mountains than previously suspected.

FURTHER DISCUSSION:

Limited acquisition of apatites within separates as well as a lack of zircon ages for some sample sites, primarily collocated samples such as RGD18-14, provide an incentive to return to mineral separates and obtain a larger sample of apatite ages along the transect sampled. The incorporation of additional apatites and zircons would help define the parameters of the onset and end of exhumation. Separately, the incorporation of K-Ar and $^{40}Ar/^{39}Ar$ thermochronology upon collected hornblende, muscovite, biotite, and potassium feldspar, would provide a more complete thermal history as these thermochronometers record events up to ~580°C. These thermochronometers would allow us to determine whether exhumation was constrained to a singular, rapid event during the mid-Miocene or if exhumation within the area was longer lived. The $^{40}Ar/^{3}9Ar$ data is currently being collected by colleagues at the University of Dayton, and the search for apatites will continue here at CU. With more constraints on the timing of events,

forward and inverse modeling of He dates using HeFTy will provide a more comprehensive thermal history for the northern Ruby Mountains.

Table 1. Results of Apatite (U/Th)/He Analysis

Sample Name	Length (μm)	Width (μm)	Rs (μm)	4He (nmol/g)	U (ppm)	Th (ppm)	Sm (ppm)	eU	Re (%)	Ft	Age (Ma)	Analytic Unc. (Ma)2σ
RGD18-15_a1	218.8	107.8	51.35	2.554	23.05	0.92	31.30	23.3	**97.0**	0.731	27.41	1.09
RGD18-15_a2	102.1	133.7	48.19	1.550	21.10	0.78	32.40	21.3	100.0	0.720	18.47	1.31
RGD18-15_a3	232.2	174.1	60.83	2.510	26.69	1.25	30.78	27.0	**96.0**	0.775	21.99	0.97
RGD18-15_a4	234.1	183.7	73.67	1.169	18.45	0.32	31.51	18.5	99.9	0.812	14.18	0.70
RGD18-15_a5	207.6	101.0	52.29	2.076	22.26	1.06	28.11	22.5	**99.9**	0.736	22.92	1.41

Table 4. Results of Zircon (U-Th)/He Analysis

Full Sample Name	Length 1 (μm)	Width 1 (μm)	Length 2 (μm)	Width 2 (μm)	Radius (μm)	4He (nmol/g)	U (ppm)	Th (ppm)	Sm (ppm)	eU	Re (%)	Ft	Corrected Date (It) (Ma)	Analytic Unc. (Ma)2σ
RGDJ18-13A_z01	367.4	91.6	370.0	125.1	69.37	81.983	1004.98	120.87	0.93	1033.4	**99.8**	0.837	17.56	0.54
RGDJ18-13A_z02	242.2	99.1	245.8	103.0	62.77	13.269	242.89	17.82	0.23	247.1	**99.0**	0.822	12.12	0.75
RGDJ18-13A_z03	285.4	91.7	285.6	117.0	65.35	21.478	309.06	19.59	0.17	313.7	**98.3**	0.828	15.33	0.38
RGDJ18-13B_z01	281.3	101.4	286.1	85.0	59.91	11.407	176.47	36.69	0.45	185.1	**98.9**	0.811	14.09	0.50
RGDJ18-13B_z02	214.5	91.3	212.1	87.6	55.07	22.044	313.20	30.80	0.16	320.4	**99.6**	0.796	16.02	0.55
RGDJ18-13B_z03	195.5	98.2	191.3	90.5	55.61	22.190	360.84	38.78	2.73	370.0	**99.5**	0.798	13.94	1.14
RGDJ18-13B_z05	173.6	97.5	176.1	87.4	52.94	46.637	123.42	46.21	0.40	134.3	100.0	0.786	81.37	2.83
RGDJ18-14A_z01	105.5	60.8	110.1	61.3	34.17	319.937	117.68	93.18	2.14	139.6	100.0	0.674	588.94	19.34
RGDJ18-14B_z01	247.2	111.1	247.1	106.0	66.04	0.870	2.95	3.89	6.63	3.9	**99.7**	0.822	49.75	2.33
RGDJ18-14B_z02	236.0	100.0	234.0	108.2	63.12	6.264	13.99	13.32	12.59	17.1	100.0	0.816	81.99	2.88
RGDJ18-14B_z03	186.0	78.9	186.4	101.4	52.50	1.043	13.39	0.68	14.97	13.5	99.9	0.787	17.95	1.79
RGDJ18-14B_z04	266.0	107.1	268.5	97.1	64.10	0.711	3.54	0.53	3.53	3.7	**99.1**	0.823	43.22	2.34
RGDJ18-14B_z05	326.3	127.8	326.8	133.2	81.28	63.436	765.14	127.43	0.32	795.1	**98.0**	0.859	17.21	0.44
RGDJ18-15_z01	418.5	123.8	421.5	116.7	79.17	24.246	317.12	37.55	0.20	325.9	**93.7**	0.856	16.10	0.45
RGDJ18-15_z02	406.0	79.4	405.4	92.8	58.76	40.891	504.26	158.70	1.61	541.6	**98.3**	0.806	17.35	0.60
RGDJ18-15_z03	332.5	80.3	337.5	100.5	59.08	21.954	340.06	25.88	0.36	346.1	**98.2**	0.810	14.51	0.70
RGDJ18-16A_z01	301.0	117.5	280.0	142.4	79.05	104.783	1185.60	22.04	1.02	1190.8	100.0	0.857	23.51	0.72
RGDJ18-16A_z03	252.4	88.6	252.7	91.6	57.33	180.294	2142.35	33.78	1.75	2150.3	100.0	0.806	22.40	0.52
RGDJ18-16A_z04	218.3	89.2	218.6	88.7	55.18	181.506	2112.80	116.18	0.73	2140.1	98.0	0.797	19.73	0.40
RGDJ18-16B_z01	244.2	92.2	247.5	81.6	55.35	84.748	977.39	168.31	0.48	1016.9	100.0	0.796	19.39	0.51
RGDJ18-16B_z02	286.4	122.4	288.2	137.7	78.23	32.126	362.68	54.74	0.24	375.5	99.8	0.854	18.56	0.54
RGDJ18-16B_z03	164.9	96.4	169.1	101.4	54.27	0.002	0.54	0.15	0.00	0.6	43.7	0.792	0.64	4.94
RGDJ18-17A_z01	377.5	222.2	387.9	264.5	128.11	6.462	70.76	22.74	0.36	76.1	**99.5**	0.909	17.30	0.70
RGDJ18-17A_z02	588.5	105.1	589.0	110.4	74.93	93.866	1014.23	76.42	0.33	1032.2	**98.9**	0.848	19.87	0.39
RGDJ18-17A_z03	406.6	239.2	391.0	166.7	114.30	1.772	18.77	3.97	5.33	19.7	100.0	0.897	18.54	0.61
RGDJ18-18_z01	462.7	131.4	466.8	193.2	100.33	34.618	402.77	88.52	0.29	423.6	100.0	0.885	17.12	0.42
RGDJ18-18_z02	376.0	119.8	380.2	109.9	75.26	33.599	423.96	85.47	0.26	444.0	**89.4**	0.848	16.54	0.57
RGDJ18-18_z03	500.3	199.5	498.3	198.7	124.13	34.185	368.17	66.74	0.16	383.9	**94.2**	0.907	18.20	1.04
RGDJ18-19_z01	194.1	99.5	190.7	110.3	59.42	11.049	120.63	47.22	0.23	131.7	**99.6**	0.808	19.22	0.62
RGDJ18-19_z02	268.1	144.2	269.5	118.0	76.54	4.613	56.10	16.24	0.24	59.9	**99.7**	0.850	16.78	0.43
RGDJ18-19_z03	182.7	73.0	182.3	91.9	49.14	4.749	67.00	22.28	0.29	72.2	**99.4**	0.771	15.80	3.54
RGDJ18-20_z01	218.2	91.0	212.7	75.3	51.81	200.737	1912.84	2703.59	2.42	2548.2	**98.8**	0.777	18.75	0.64
RGDJ18-20_z02	259.5	88.7	277.5	63.3	48.81	37.068	431.67	429.11	1.11	532.5	100.0	0.765	16.83	0.31
RGDJ18-20_z03	202.7	123.5	216.8	154.5	77.57	43.090	435.87	449.16	0.68	541.4	100.0	0.850	17.32	0.45

SOURCES:

1. Camilleri, P.A., and Chamberlain, K.R., 1997, Mesozoic tectonics and metamorphism in the Pequop Mountains and Wood Hills region, northeast Nevada: Implications for the architecture and evolution of the Sevier orogen (vol 109, pg 74, 1997): Geological Society of America Bulletin, v. 109, no. 4, p. 504.
2. Colgan, J.P., Howard, K.A., Fleck, R.J., and Wooden, J.L., 2010, Rapid middle Miocene extension and unroofing of the southern Ruby Mountains, Nevada: Tectonics, v. 29, no. 6, p. TC6022.
3. Dallmeyer, R.D., Snoke, A.W., and McKee, E.H., 1986, The Mesozoic-Cenozoic tectonothermal evolution of the Ruby Mountains, East Humboldt Range, Nevada: A Cordilleran metamorphic core complex: Tectonics, v. 5, no. 6, p. 931–954.
4. Ehlers T.A. and Farley, K.A. Apatite (U-Th)/He thermochronometry: methods and applications to problems in tectonic and surface processes, Earth and Planetary Science Letters 206, 1-14 (2003).
5. Farley, K.A. (U-Th)/He dating: Techniques, calibrations, and applications, in: Noble Gases in Geochemistry and Cosmochemistry, REVIEWS IN MINERALOGY & GEOCHEMISTRY 47, pp. 819-844 (2002).
6. Flowers, R. M., Shuster, D. L., Wernicke, B. P., and Farley, K. A., 2007, Radiation damage control on apatite (U-Th)/He dates from the Grand Canyon region, Colorado Plateau: Geology, v. 35, n. 5, p. 447–450, http://dx.doi.org/10.1130/G23471A.1
7. Flowers, R. M., R. A. Ketcham, D. L. Shuster, and K. A. Farley (2009), Apatite (U-Th)/He thermochronometry using radiation damage accumulation and annealing model, Geochim. Cosmochim. Acta, 73, 2347–2365.
8. Hallett, B.W., and Spear, F.S.,2014, The P-T history of anatectic pelites of the northern East Humboldt Range, Nevada: Evidence for tectonic loading, de- compression, and anatexis. Journal of Petrology, 55, 3–36.
9. Hallett, B.W., and Spear, FS., 2015, Monazite, zircon, and garnet growth in migmatitic pelites as a record of metamorphism and partial melting in the East Humboldt Range, Nevada: American Mineralogist, v. 100, p. 951-972.
10. Henry, C.D., McGrew, A.J., Colgan, J.P., Snoke, A.W., and Brueseke, M.E., 2011, Timing, distribution, amount, and style of Cenozoic extension in the northern Great Basin (J. Lee & J. P. Evans, Eds.): GSA Field Guide, v. 21, p. 27–66.

11. Hiess, J., Condon, D.J., Mclean, N., and Noble, S.R., 2012, U-238/U-235 Systematics in Terrestrial Uranium-Bearing Minerals: Science, v. 335, p. 1610–1614, doi: 10.1126/science.1215507.
12. Hodges, K. V, Snoke, A.W., and Hurlow, H.A., 1992, Thermal Evolution of a Portion of the Sevier Hinterland - the Northern Ruby Mountains-East Humboldt Range and Wood Hills, Northeastern Nevada: Tectonics, v. 11, no. 1, p. 154–164.
13. Hudec, M.R., 1992, Mesozoic Structural and Metamorphic History of the Central Ruby Mountains Metamorphic Core Complex, Nevada: Geological Society of America Bulletin, v. 104, no. 9, p. 1086–1100.
14. Hurlow, H.A., Snoke, A.W., and Hodges, K. V, 1991, Temperature and pressure of mylonitization in a Tertiary extensional shear zone, Ruby Mountains-East Humboldt Range, Nevada: Tectonic implications: Geology, v. 19, no. 1, p. 82.
15. Ketcham, R. A., Gautheron, C., & Tassan-Got, L. (2011). Accounting for long alpha-particle stopping distances in (U-Th-Sm)/He geochronology: Refinement of the baseline case. Geochmica Et Cosmochimica Acta, 75(24), 7779–7791. http://doi.org/10.1016/j.gca.2011.10.011
16. McGrew, A.J., and Snoke, A.W., 2015, Geology of the Welcome Quadrangle and adjacent part of the Wells Quadrangle, Elko County, Nevada: Nevada Bureau of Mines and Geology Map 184, 1:24,000 with 1:12,000 inset, companion text, 40 p.
17. McGrew, A.J., Peters, M.T., and Wright, J.E., 2000, Thermobarometric constraints on the tectonothermal evolution of the East Humboldt Range metamorphic core complex, Nevada: Geological Society of America Bulletin, v. 112, no. 1, p. 45–60.
18. Stockli, D.F., 2005, Application of Low-Temperature Thermochronometry to Extensional Tectonic Settings: Reviews in Mineralogy and Geochemistry, v. 58, no. 1, p. 411–448.
19. Snoke, A.W., Howard, K.A., McGrew, A.J., Burton, B.R., Barnes, C.G., Peters, M.T., and Wright, J.E., 1997, The grand tour of the Ruby–East Humboldt metamorphic core complex, northeastern Nevada— part 1, Introduction & Road Log, in Link, P.K., and Kowallis, B.J. , editors, Proterozoic to recent stratigraphy, tectonics, and volcanology, Utah, Nevada, southern Idaho and central Mexico: Provo, Utah, Brigham Young University Geology Studies, v. 42, Part 1, p. 225–269.
20. Thorman, C.H., and L.W. Snee, Thermochronology of metamorphic rocks in the Wood Hills and Pequop Mountains, northeastern Nevada (abstract), Geol. Soc. Am. Abstr. Programs, 20, 18, 1988

21. Wolf R. A., Farley K. A. and Kass D. M. (1998) Modeling of the temperature sensitivity of the apatite (U-Th)/He thermochro- nometer. Chemical Geology 148, 105–114.